Deep Subaru Hyper Suprime-Cam Observations of Milky Way Satellites Columba I and Triangulum II*

Jeffrey L. Carlin[1] , David J. Sand[2,3] , Ricardo R. Muñoz[4], Kristine Spekkens[5,6] , Beth Willman[7] , Denija Crnojević[2] ,
Duncan A. Forbes[8], Jonathan Hargis[9], Evan Kirby[10] , Annika H. G. Peter[11] , Aaron J. Romanowsky[12,13] , and Jay Strader[14]

[1] LSST, 950 North Cherry Avenue, Tucson, AZ 85719, USA; jcarlin@lsst.org
[2] Texas Tech University, Physics & Astronomy Department, Box 41051, Lubbock, TX 79409-1051, USA
[3] Department of Astronomy/Steward Observatory, 933 North Cherry Avenue, Rm. N204, Tucson, AZ 85721-0065, USA
[4] Departamento de Astronomía, Universidad de Chile, Casilla 36-D, Santiago, Chile
[5] Department of Physics, Engineering Physics and Astronomy, Queen's University, Kingston, ON K7L 3N6, Canada
[6] Department of Physics, Royal Military College of Canada, P.O. Box 17000, Station Forces, Kingston, ON K7L 7B4, Canada
[7] LSST and Steward Observatory, 933 North Cherry Avenue, Tucson, AZ 85721, USA
[8] Centre for Astrophysics and Supercomputing, Swinburne University, Hawthorn, VIC 3122, Australia
[9] Space Telescope Science Institute, 3700 San Martin Drive, Baltimore, MD 21218, USA
[10] California Institute of Technology, 1200 East California Boulevard, MC 249-17, Pasadena, CA 91125, USA
[11] CCAPP, Department of Physics, and Department of Astronomy, The Ohio State University, Columbus, OH 43210, USA
[12] Department of Physics and Astronomy, San José State University, One Washington Square, San José, CA 95192, USA
[13] University of California Observatories, 1156 High Street, Santa Cruz, CA 95064, USA
[14] Department of Physics and Astronomy, Michigan State University, East Lansing, MI 48824, USA

Abstract

We present deep, wide-field Subaru Hyper Suprime-Cam photometry of two recently discovered satellites of the Milky Way (MW): Columba I (Col I) and Triangulum II (Tri II). The color–magnitude diagrams of both objects point to exclusively old and metal-poor stellar populations. We re-derive structural parameters and luminosities of these satellites, and find $M_{\rm V,Col\,I} = -4.2 \pm 0.2$ for Col I and $M_{\rm V,Tri\,II} = -1.2 \pm 0.4$ for Tri II, with corresponding half-light radii of $r_{\rm h,Col\,I} = 117 \pm 17$ pc and $r_{\rm h,Tri\,II} = 21 \pm 4$ pc. The properties of both systems are consistent with observed scaling relations for MW dwarf galaxies. Based on archival data, we derive upper limits on the neutral gas content of these dwarfs, and find that they lack H I, as do the majority of observed satellites within the MW virial radius. Neither satellite shows evidence of tidal stripping in the form of extensions or distortions in matched-filter stellar density maps or surface-density profiles. However, the smaller Tri II system is relatively metal-rich for its luminosity (compared to other MW satellites), possibly because it has been tidally stripped. Through a suite of orbit simulations, we show that Tri II is approaching pericenter of its eccentric orbit, a stage at which tidal debris is unlikely to be seen. In addition, we find that Tri II may be on its first infall into the MW, which helps explain its unique properties among MW dwarfs. Further evidence that Tri II is likely an ultra-faint dwarf comes from its stellar mass function, which is similar to those of other MW dwarfs.

Key words: galaxies: dwarf – galaxies: individual (Columba I, Triangulum II) – galaxies: photometry – Galaxy: halo – Local Group

1. Introduction

The number of known Milky Way (MW) satellites has been increasing rapidly over the past several years due to the availability of large-area, deep, high-precision photometric catalogs from imaging surveys such as the Sloan Digital Sky Surveys (SDSS; York et al. 2000; Abazajian et al. 2009; Alam et al. 2015), ATLAS (Shanks et al. 2015), the Panoramic Survey Telescope and Rapid Response System (Pan-STARRS; Chambers et al. 2016), the Dark Energy Survey (DES; Dark Energy Survey Collaboration 2005; Dark Energy Survey Collaboration et al. 2016), and other surveys employing the Dark Energy Camera (e.g., MagLiteS: Drlica-Wagner et al. 2016; Drlica-Wagner & MagLiteS Team 2017; SMASH: Nidever et al. 2017). Many of these new discoveries fall into the "ultra-faint dwarf" (UFD) category (e.g., Willman et al. 2005; Belokurov et al. 2006, 2007; Zucker et al. 2006a, 2006b; Walsh et al. 2007; Bechtol et al. 2015; Kim et al. 2015; Kim & Jerjen 2015; Koposov et al. 2015; Laevens et al. 2015a; Martin

et al. 2015; Drlica-Wagner et al. 2016; Torrealba et al. 2016), with luminosities as low as a few hundred $L_\odot$. The UFDs are apparently the most dark matter (DM) dominated systems known (e.g., Simon & Geha 2007), though the so-called "ultra-diffuse galaxies" may have extremely high DM fractions as well (e.g., Koda et al. 2015; Beasley et al. 2016; van Dokkum et al. 2016; Zaritsky 2017). Because there are UFDs that are fainter than (and as small as) bright globular clusters (GCs), the line between star clusters and dwarf galaxies has become blurred. Willman & Strader (2012) argued that a "galaxy" should be defined as an object with properties that cannot be readily explained by a combination of Newtonian gravity and baryons, whereas Forbes & Kroupa (2011) advocated a dynamical criterion and/or the presence of complex stellar populations to define a galaxy. Evidence that the UFDs differ from GCs in ways that satisfy these definitions of a galaxy is seen in the form of metallicity spreads among their stars (such that they must have had deep potential wells to retain their gas for extended periods) and large velocity dispersions (suggesting their kinematics are dominated by DM).

As the most DM-dominated, chemically pristine objects in the Universe (e.g., Muñoz et al. 2006; Brown et al. 2012; Kirby

---

et al. 2013), the UFDs are important laboratories in which to seek clues to the nature of DM (via, e.g., searching for gamma-ray signals due to DM particle annihilation; Albert et al. 2017). Given that tidal forces are likely to have shaped their properties (e.g., Peñarrubia et al. 2008), it is also curious that Local Group dwarfs follow well-determined scaling relations (for several examples, see McConnachie 2012). Muñoz et al. (2012) showed that the structural parameters (e.g., size, stellar density, luminosity) of UFDs derived using small numbers of stars are biased, so it is important that we measure their properties via deep imaging and precise photometry. With imaging over a sufficient area around a given dwarf, one can also search for signs of tidal disruption in the stellar density (e.g., Sand et al. 2009; Muñoz et al. 2010; Sand et al. 2012). Deep follow-up photometry of the new MW satellites has already led to other surprises, including the smallest galaxy known to host its own star cluster in Eridanus II (Crnojević et al. 2016), which has yielded its own constraints on DM properties (e.g., Brandt 2016; Amorisco 2017; Contenta et al. 2017a).

In this contribution, we detail our deep Subaru+Hyper Suprime-Cam (HSC) imaging around two recently discovered UFD candidates—Columba I (Col I) and Triangulum II (Tri II). Col I is a distant ($d \sim 180$ kpc) UFD candidate that was discovered as an overdensity of red giant branch (RGB) stars in DES Year 2 data (Drlica-Wagner et al. 2015). Its properties as measured by Drlica-Wagner et al. (2015) are fairly typical of Local Group UFDs, with a half-light radius of ~ 100 pc and luminosity $\sim 5 \times 10^3 L_\odot$ ($M_V \approx -4.5$). This candidate dwarf shows a prominent blue horizontal branch (BHB) and a sparsely populated RGB. Our aim in the current work is to derive structural parameters by probing nearly to the main sequence turnoff (MSTO) of Col I, which provides a much larger sample of stars with which to robustly determine the properties of this distant, faint dwarf candidate. We also search for tidally induced distortions in its outer regions.

Tri II was discovered by Laevens et al. (2015b) as a stellar excess at a distance of ~ 30 kpc in the PanSTARRS1 database, and confirmed with deeper Large Binocular Telescope (LBT) imaging. Laevens et al. found Tri II to be extremely faint ($M_V \sim -1.8$, or $L \sim 450 L_\odot$) and compact ($r_h \sim 30$ pc), with very few RGB stars, but apparently metal-poor stellar populations. There have been multiple spectroscopic follow-up programs of Tri II (Kirby et al. 2015, 2017; Martin et al. 2016; Venn et al. 2017). While there is some debate as to its dynamical status and DM content (e.g., Martin et al. 2016; Kirby et al. 2017), the apparent presence of a metallicity spread is indicative of a dwarf galaxy origin (Kirby et al. 2017). Our extremely deep imaging may shed light on the equilibrium status of this system.

2. Observations and Data Reduction

We observed Col I on 2016 February 10 and Tri II on 2016 February 9 with HSC (Miyazaki et al. 2012) on the Subaru 8.2 m telescope during scheduled time that was unusable for our Magellanic Analogs Dwarf Companions And Stellar Halos Local Volume galaxies program (see Carlin et al. 2016). HSC has a $1°.5$ diameter field of view that easily encompasses the new MW satellites, which are typically a few arcminutes in size, and allows for a search for extended low surface-brightness features that may have been missed in the discovery data. Seeing during the Tri II observations was $\sim 0''.8$–$1''.0$, under photometric conditions. For the Col I observations we

had $\sim 0''.7$–$1''.0$ seeing, under clear, photometric skies. Exposure times were 12×150 s in i and 8×300 s in g for both Tri II and Col I, reaching 5σ limiting depths of $g \sim 26.9$ and $i \sim 25.8$ for Tri II, and $g \sim 27.1$, $i \sim 25.9$ for Col I in the reduced co-added frames.

The data were reduced using *hscPipe* (Bosch et al. 2017), a modified version of the LSST software stack (Ivezic et al. 2008; Jurić et al. 2015), including standard processing steps, co-adding of the individual (dithered) frames, and PSF photometry. Our final stellar catalog included all objects classified as "point-like" by the *hscPipe* star/galaxy classifier, which is based on the difference between PSF and cmodel[15] magnitudes for each object (similar to classification_extendedness; e.g., Aihara et al. 2017; Huang et al. 2017).

2.1. Catalogs and Color–Magnitude Diagrams

We calibrate the photometry by matching to the Pan-STARRS (PS1) survey (Chambers et al. 2016; Flewelling et al. 2016; Magnier et al. 2016), and fitting transformations in g and i that include both a magnitude and color dependence (including only stars between $18 < g < 21$ and $17.5 < i < 20.5$ in the fits). We apply extinction corrections based on the Schlafly & Finkbeiner (2011) modifications of the Schlegel et al. (1998) reddening maps. The mean reddening values along the lines of sight to Col I and Tri II are $E(B - V) = 0.03$ and 0.07, respectively. All photometry used throughout this work has been calibrated onto the PS1 system and corrected for line of sight extinction.

We present the final color–magnitude diagrams (CMDs) of Col I in Figure 1 and Tri II in Figure 2. For Col I's CMD, we include stars within $2'.2$ (our measured half-light radius; see Section 4) of the dwarf's center. Candidate blue horizontal-branch stars (BHBs) within $5'$ of the Col I center are displayed as large open diamonds, highlighting the prominent BHB of this galaxy. Col I shows a narrow and well-defined RGB, and a clear MSTO that mingles with unresolved background galaxies at magnitudes $i_0 \gtrsim 25.5$. The right panel of Figure 1 encodes the number density of stars in the same region as the left panel, after subtracting the average density in each color/mag bin from four equal-area background fields well outside the body of Col I. The MSTO is much clearer in this Hess diagram, which accounts for the average number of contaminating background galaxies.

Figure 2 shows the CMD of stars within $2'.5$ of Tri II, which reaches $\gtrsim 4$ mag below the MSTO. The main sequence is narrow and well-defined, with a sparsely populated RGB and no evidence for a BHB population. (Note that the bright end of the RGB is cut off because our deep data saturate at $i_0 \sim 18$.) In the background-subtracted Hess diagram (right panel of Figure 2), the main sequence is clear down to the limiting magnitude of our data at $i_0 \gtrsim 25$.

3. Distances

We derive the distance to Col I using the prominent BHB. We estimate the distance by performing a least-squares fit of our Col I BHB stars (large diamonds in Figure 1) to the empirical BHB ridgeline of the metal-poor ([Fe/H] = -2.34; Carretta et al. 2009) GC NGC 7078 (M15) determined by Bernard et al. (2014) using PanSTARRS photometry (assuming
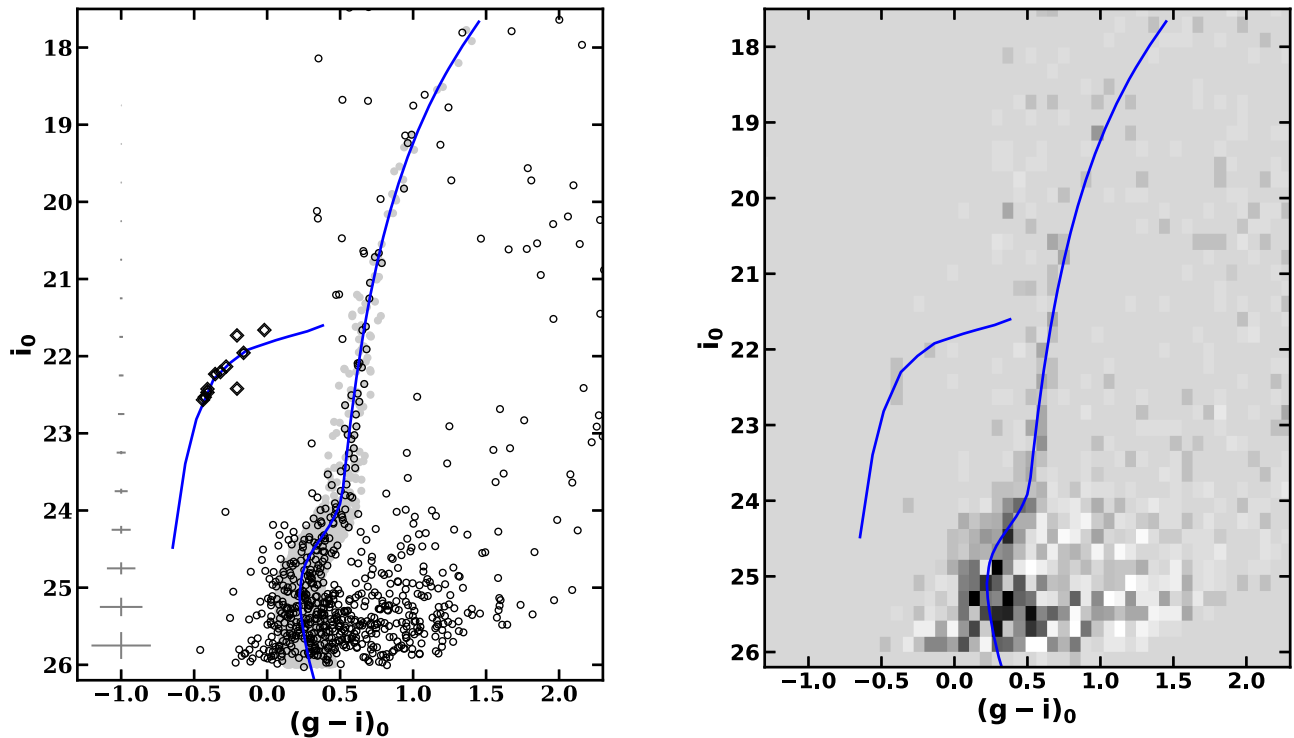
---

[15] http://www.sdss3.org/dr10/algorithms/magnitudes.php#cmodel

Figure 1. Left: color–magnitude diagram showing (open circles) all well-measured (magnitude errors less than 0.2) point sources within $2'.2$ (our measured half-light radius) of the center of Col I. Large open diamonds are BHB candidates, for which we include sources out to $5'$ from the center. Magnitudes have been calibrated to PanSTARRS public data (Chambers et al. 2016). Large gray points are stars within $12'$ of the center of Col I, selected by our isochrone filter, which constitute the sample used to derive structural parameters. Overplotted as a blue line is the PanSTARRS ridgeline for globular cluster NGC 7078 (M15) from Bernard et al. (2014), shifted to a distance modulus of $m - M = 21.31$ that we derived by fitting the M15 BHB ridgeline to our Col I data. Median photometric errors in 0.5 mag bins are shown along the left side of the figure. Right: CMD Hess diagram of the same field of view shown in the left panel, but with the average density of four equal-area background fields subtracted. The MSTO of Col I stands out more clearly once the background is removed. The ridgeline of the old (>10 Gyr), metal-poor ([Fe/H] ~ -2.34) cluster NGC 7078 closely matches the stellar population of Col I; hence, Col I must also consist of a predominantly old, metal-poor population.

a distance modulus of $m - M = 15.39$ to NGC 7078, here and throughout this work). We find a best-fitting distance modulus to Col I of $m - M = 21.31 \pm 0.11$, corresponding to a distance of $d_{\mathrm{Col\,I}} = 183 \pm 10$ kpc. In Figure 1, we overplot the PanSTARRS ridgeline for the main sequence and RGB populations of NGC 7078, shifted to $m - M = 21.31$; the MSTO and RGB of Col I very closely match the ridgelines.

To determine the distance to Tri II, for which our data reach >3 mag below the MSTO, we perform a least-squares fit of the NGC 7078 ridgeline to all Tri II candidates with $i_0 < 24$ (where the Tri II main sequence is well separated from the unresolved background galaxy contamination, and below which the NGC 7078 ridgeline is unconstrained by PS1 data). This yields a distance modulus of $m - M = 17.27 \pm 0.11$, corresponding to $d_{\mathrm{Tri\,II}} = 28.4 \pm 1.6$ kpc, which is similar to the distance of 30 ± 2 kpc estimated by Laevens et al. (2015b). This corresponds to a Galactocentric distance of $d_{\mathrm{GC,Tri\,II}} \approx 34.5$ kpc (assuming the Sun is 8 kpc from the Galactic center) at the Tri II Galactic coordinates of $(l, b) = (140°.9, -23°.8)$. The NGC 7078 BHB ridgeline, shifted to $m - M = 17.27$, is overplotted in each panel of Figure 2, with an old, metal-poor, alpha-enhanced Dartmouth isochrone shown in both panels to better illustrate the main sequence.

4. Structural Parameters and Luminosities

We estimate the structural parameters of both UFDs using the maximum likelihood method of Martin et al. (2008) as

implemented by Sand et al. (2009) and Muñoz et al. (2010). We include stars with $i_0 < 26.0$ that are within 12 arcmin of the center of Col I, selected within a filter centered on the NGC 7078 ridgeline, that spans ± 0.05 mag at $i_0 = 18.0$, expanding linearly in width to ± 0.15 mag at $i_0 = 25.0$ (this ends up being 0.164 mag wide at $i_0 = 26$; the selection includes a total of 3242 stars, shown as gray points in Figure 1). For Tri II, we use a similar filter, but centered on a Dartmouth isochrone (Dotter et al. 2008) with age 13 Gyr, [Fe/H] = -2.0, and [α/Fe] = 0.4, with filter width increasing from ± 0.05 mag at $i_0 = 18$ to ± 0.2 mag at $i_0 = 25$. We include isochrone-filtered stars within $r < 15'$ of the Tri II center with magnitudes $i_0 < 25$ (2550 input stars in total; gray points in Figure 2). The resulting structural parameters are summarized in Table 1. These include the central position, half-light radius (r_h), ellipticity (ϵ), and position angle θ from fitting an exponential, and the King (1962) model core and tidal radii (r_c and r_t, respectively). Our deep, large-area data set satisfies all of the conditions (large field of view, total number of stars, and central-to-background density contrast) found by Muñoz et al. (2012) to be necessary for deriving accurate structural parameters.

Luminosities were derived using the technique of Sand et al. (2009). To do so, we generate synthetic stellar populations using IAC-Star (Aparicio & Gallart 2004),[16] sampling from a power-law IMF with slope -1.3 for $0.1\,M_\odot < M < 0.5\,M_\odot$ and -2.3 for $0.5\,M_\odot < M < 120\,M_\odot$ until we have 50,000 synthetic stars
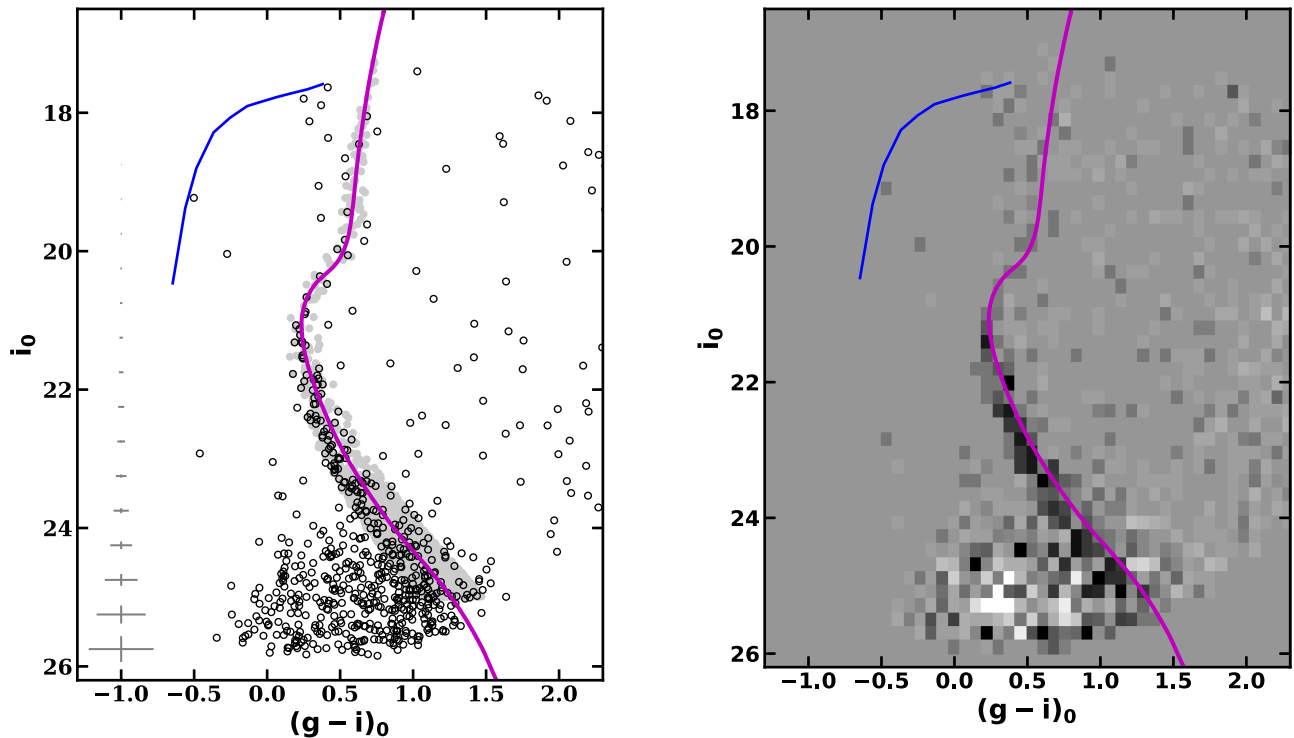

Figure 2. Left: color–magnitude diagram of point sources within 2.'5 (roughly our measured half-light radius) of the center of Tri II as open circles. Magnitudes have been calibrated to PanSTARRS public data. As in Figure 1, large gray points illustrate the sample selection for structural parameter derivation; for Tri II this includes stars within 15' of the center. Overplotted as a blue line is the PanSTARRS BHB ridgeline for globular cluster NGC 7078 (M15) from Bernard et al. (2014), shifted by a distance modulus of $m - M = 17.27$ that we derived by fitting the M15 main sequence ridgeline to our Tri II data. Because the empirical M15 ridgeline only traces the upper main sequence, we use a theoretical isochrone for Tri II analysis. We have overlaid a Dartmouth isochrone (magenta sequence; Dotter et al. 2008) with age 13 Gyr, [Fe/H] = −2.0, and [α/Fe] = 0.4, shifted to the distance of Tri II. This is the isochrone that we used to filter stars for deriving the structural parameters. Median photometric errors in 0.5 mag bins are shown along the left side of the figure. Right: CMD Hess diagram of the same field of view shown in the left panel, but with the average density of four equal-area background fields subtracted. The main sequence of Tri II is well defined to $i_0 \sim 25$ once the background is removed.

<div style="text-align:center">

Table 1
Properties of Col I and Tri II

</div>

Parameter	Col I	Tri II
R. A. (hh:mm:ss)	05:31:25.67 ± 8.''0	02:13:17.34 ± 14.''4
Decl. (dd:mm:ss)	−28:02:33.1 ± 11.''4	+36:10:18.9 ± 9.''7
$m - M$ (mag)	21.31 ± 0.11	17.27 ± 0.11
d (kpc)	183 ± 10	28.4 ± 1.6
M_V (mag)	−4.2 ± 0.2	−1.2 ± 0.4
$r_{h,exp}$ (arcmin)	2.2 ± 0.2	2.5 ± 0.3
$r_{h,exp}$ (pc)	117 ± 17	21 ± 4
ϵ	0.3 ± 0.1	0.3 ± 0.1
θ (degree)	24° ± 9°	73° ± 17°
$\langle \mu \rangle_{eff, v}$[a] (mag arcsec^{-2})	29.0 ± 0.6	28.2 ± 0.8
$r_{c,King}$ (arcmin)	2.1 ± 0.6	2.1 ± 0.6
$r_{c,King}$ (pc)	112 ± 40	17 ± 6
$r_{t,King}$ (arcmin)	8.9 ± 2.5	11.8 ± 2.7
$r_{t,King}$ (pc)	472 ± 160	97 ± 27
$M_{HI}(M_\odot)$	<1.2 × 10^4	<3.1 × 10^2
$M_{HI}/L_V (M_\odot/L_\odot)$	<3.1	<1.2

Note.
[a] Average surface brightness within the half-light radius.

in our catalogs. For both UFDs, we use an old (13 Gyr), metal-poor ($Z = 0.0001$) stellar population. We then randomly sample the same number of stars as were included in our observed data sets (201 and 213 stars for Col I and Tri II, respectively) from

these catalogs, within the magnitude ranges included in our parameter estimations. The derived luminosities represent the average and its standard deviation of the total flux from over 1000 samples for each dwarf. This accounts for the effects of CMD shot-noise. The resulting luminosities are tabulated in Table 1; we discuss the properties of each galaxy below.

4.1. Col I

Our deep observations, which reach beyond the MSTO (at $i_0 \sim 25.5$), confirm that Col I has a position in the size–luminosity plane (Figure 5) consistent with being a distant, metal-poor UFD. We find an extremely narrow RGB and a prominent BHB (Figure 1). Unlike Drlica-Wagner et al. (2015), we see no obvious evidence of red horizontal branch stars. In fact, Col I appears to consist of a single, metal-poor stellar population, with no age or metallicity spread broadening its RGB. We find that the PS1 ridgeline of GC NGC 7078 ([Fe/H] = −2.34; Carretta et al. 2009) is an excellent match to Col I, including its BHB, which implies that Col I must be old and metal-poor as well. We derive a distance $d_{Col I} = 183 \pm 10$ kpc (see Section 3), which agrees with the estimate of 182 ± 18 kpc from its discovery in DES (Drlica-Wagner et al. 2015). Likewise, our deeper, higher-quality data yield a more precise measurement of the half-light radius: $r_{h,Col I} = 117 \pm 17$ pc, which is consistent with the radius (103 ± 25 pc) measured by Drlica-Wagner et al. (2015). Col I is rather round ($\epsilon \approx 0.3 \pm 0.1$), suggesting that this UFD shows no evidence of recent tidal stripping. This is further confirmed in the density map (left panel of Figure 3), which
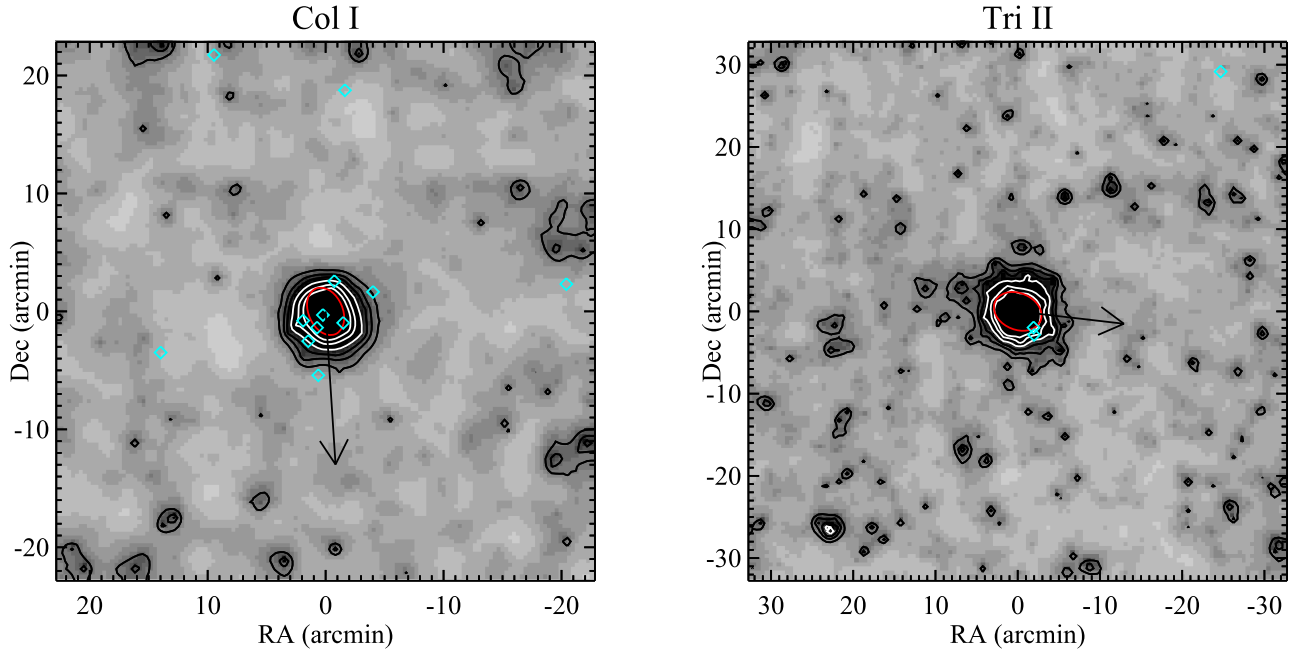
Col I

Tri II

Figure 3. Matched-filter density maps of point sources near Col I and Tri II, including sources brighter than $i_0 < 25.5$ for Col I and $i_0 < 25$ for Tri II. Bins for Col I are $20''$ in R. A. and decl., and for Tri II, $30''$. Both maps have been smoothed with an exponential kernel with $45''$ scale length. Contours denote the 3σ, 5σ, 7σ, 10σ, 15σ, and 20σ levels (though because the maps are smoothed, these should not be interpreted in the typical statistical sense). Each panel includes BHB candidates at the distance of the dwarf (i.e., stars within 0.15 mag of the NGC 7078 BHB ridgeline shifted to the appropriate distance, with $(g - i)_0 < 0$, and at $21.6 < i_0 < 22.7$ for Col I, $17.5 < i_0 < 20.5$ for Tri II) as cyan diamonds. In each panel, the red ellipse has a semimajor axis equal to our measured half-light radius, with ellipticity and position angle as determined from the maximum likelihood analysis. The arrows in each panel point in the direction of the Galactic center.
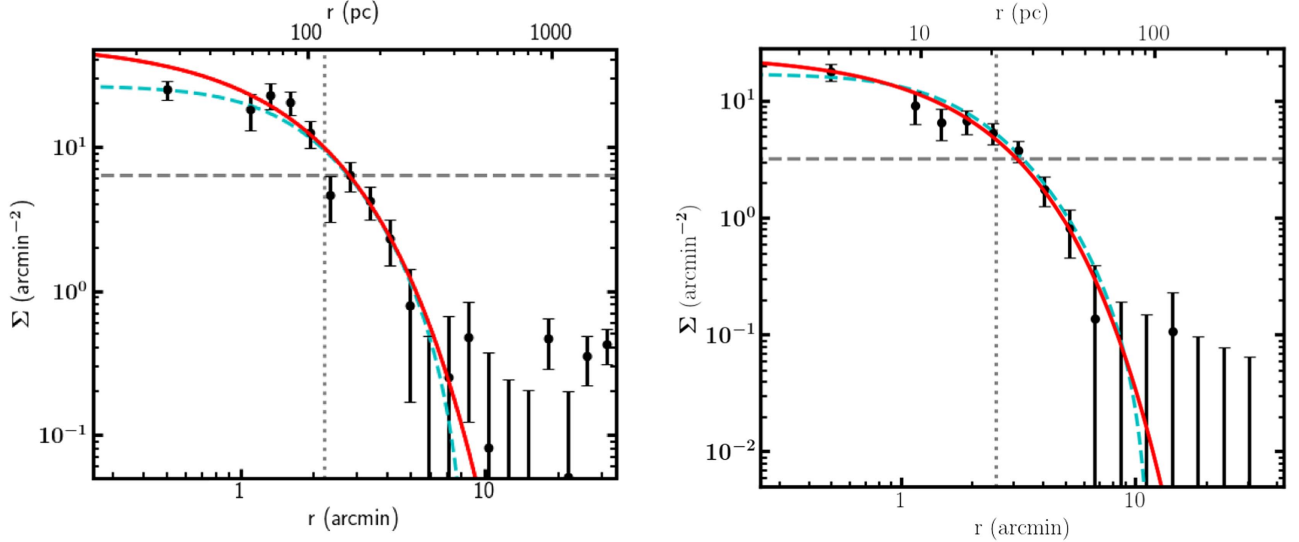
Figure 4. Left: surface density of Col I stars between $18 < i_0 < 26$, using the isochrone filter described in the text. Right: density profile of Tri II stars with $18 < i_0 < 25$, also selected with an isochrone filter. In each panel, bins are elliptical (using the derived parameters in Table 1), centered on the dwarf. The solid red lines are exponential profiles using the half-light radii of our maximum likelihood fit, and the cyan dashed lines are the best-fit King models for each dwarf. The background as determined by the maximum likelihood method has been subtracted in each panel, allowing us to see structure well below the average background level. Each panel shows the subtracted background level as a horizontal dashed gray line, and the half-light radius as a vertical dotted gray line. Neither of the dwarfs shows obvious tidal disruption in the form of a "break" from the exponential profile at large radii, to more than an order of magnitude below the background surface density.

was created using the matched-filter technique of Rockosi et al. (2002); Col I shows no irregularities in its density contours. The left panel of Figure 4 shows the surface density of Col I stars selected from the CMD as shown by the gray points in Figure 1. The background as determined by the maximum likelihood method has been subtracted, and we overlay the exponential (red curve) and King (cyan dashed curve) model fits from the maximum likelihood analysis. Both of the model

fits match the data well to surface densities at least an order of magnitude below the background level, with no obvious evidence of tidal disruption in the form of a break at large radii.

Our derived luminosity, $M_V = -4.2 \pm 0.2$, is slightly fainter than the previous estimate ($M_V = -4.5 \pm 0.2$; Drlica-Wagner et al. 2015), although the measurements are consistent within their uncertainties. Assuming a V-band absolute magnitude for the Sun of $+4.83$, our measurements imply a
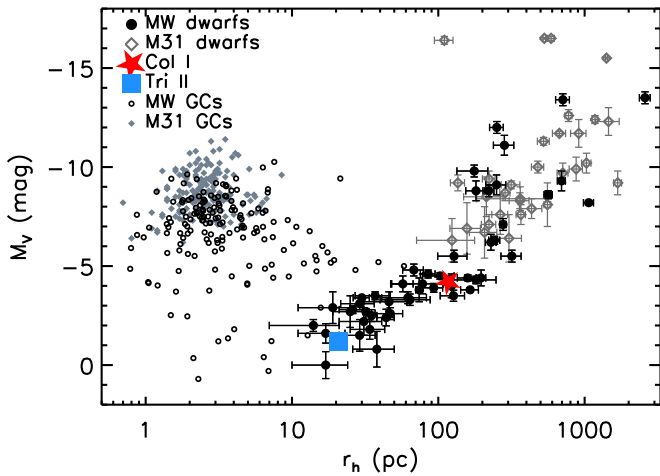
Figure 5. Size–luminosity diagram placing the Tri II (blue square) and Col I (red star) properties in context with those of the MW dwarfs (filled black circles), MW GCs (small open black circles), M31 dwarfs (open gray diamonds), and M31 GCs (small filled gray diamonds). Tri II and Col I both sit along the sequence of UFDs found in the Local Group. Points for Col I and Tri II are the size of their error ranges.

total V-band luminosity of $L_V = 4.1^{+0.8}_{-0.7} \times 10^3\,L_\odot$. We place Col I in the context of other Local Group satellites in Figure 5, which shows the size–luminosity plane for all nearby dwarf galaxies and GCs. Col I (large red star in Figure 5) lands directly on the locus defined by other MW UFDs of similar luminosity.

4.2. Tri II

Our Subaru/HSC observations probe at least 4 magnitudes deeper than Tri II's MSTO. The precise photometry reveals a narrow main sequence consistent with an old, metal-poor stellar population (Figure 2). A fit of the PS1 ridgeline for NGC 7078 provides a good match to the main sequence of Tri II, yielding a distance estimate of ∼28 ± 2 kpc. There is no clearly defined RGB locus in the CMD; indeed, it has been spectroscopically verified that most of the stars near the likely RGB location in the CMD are not members of Tri II (see Kirby et al. 2015, 2017; Martin et al. 2016). There also seem to be few, if any, BHB stars in Tri II. As expected given the spectroscopic estimates of $\langle [\mathrm{Fe/H}] \rangle \sim -2.5$ (Kirby et al. 2015, 2017; Martin et al. 2016; Venn et al. 2017), the ridgeline of the metal-poor ([Fe/H] ≈ −2.3) GC NGC 7078 matches the data well, confirming that Tri II contains a predominantly old, metal-poor stellar population.

We also checked the mass function (MF) of stars in Tri II. To do so, we fit the stellar mass as a function of i-band magnitude for a Dartmouth isochrone (Dotter et al. 2008) with [Fe/H] = −2.3 and age 13.5 Gyr, shifted to our measured distance for Tri II. Then, for each star within 3′ of the Tri II center, we assign a mass according to the mass-magnitude fit. We derive an MF as the number of Tri II stars in seven mass bins between ∼0.54 and 0.77 $M_\odot$ (magnitudes $20 < i_0 < 24$), subtracting off the average background MF from four equal-area background fields. We fit a power-law to the MF for Tri II, and find $\alpha = 2.0 \pm 0.7$. Our Tri II MF slope is consistent within the uncertainties with $\alpha_{\mathrm{Her}} = 1.2^{+0.4}_{-0.5}$ and $\alpha_{\mathrm{LeoIV}} = 1.3 \pm 0.8$ derived for the UFDs Hercules and Leo IV by Geha et al. (2013), but also consistent with a Salpeter IMF (i.e., $\alpha = 2.35$). Note, however, that we did not model the effect of unresolved

binaries on the MF, which would steepen the slope toward a more bottom-heavy MF. There is no evidence for substantial preferential loss of low-mass stars, as would be expected for relaxed GCs in the last stages of tidal dissolution (e.g., Contenta et al. 2017b).

The half-light radius of Tri II derived from our maximum likelihood analysis is $r_h = 21 \pm 4$ pc, which is consistent with the original measurement from PS1 and LBT data ($r_h = 34^{+9}_{-8}$ pc; Laevens et al. 2015b). We also find that Tri II is fainter (though in agreement within the uncertainties) than was estimated by Laevens et al. (2015b); we find $M_V = -1.2 \pm 0.4$, while the previous estimate was $M_V = -1.8 \pm 0.5$. This lower luminosity (∼260 $L_\odot$; compare to $L_V \sim 450\,L_\odot$ for the Laevens et al. value) would seemingly make Tri II an even greater outlier in the luminosity–metallicity relation for MW satellites, in which Tri II may be offset by $\gtrsim 0.5$ dex in mean metallicity from the UFD locus (e.g., Figure 7 of Kirby et al. 2017). However, given the paucity of stars with spectroscopic metallicities in Tri II, the mean metallicity is rather dependent on the membership prospects of a small number of stars (or perhaps even a single star; e.g., Kirby et al. 2017). As can be seen in Figure 5, a reduction in size along with a lower luminosity simply shifts Tri II along the size–luminosity locus of Local Group dwarfs; Tri II still lies squarely on the location populated by the lowest-luminosity MW UFDs. However, we note that when GCs are included in the size–luminosity diagram (as in Figure 5), the faintest clusters overlap the region populated by the faintest UFDs. Thus, the position of Tri II in this plane is perhaps suggestive that it is a UFD, but not a definitive indication.

One possible solution to the question of whether Tri II is a tidally disrupting UFD or a GC could be found in the surface-density distribution of Tri II stars. In our matched-filter stellar density map of Tri II (Figure 3, right panel), there is no obvious tidal distortion evident. Our measured ellipticity (Table 1) of $\epsilon = 0.3 \pm 0.1$ already suggests that Tri II is fairly round; the lack of extension in Figure 3 would seem to rule out strong/recent tidal disruption in this system. As another check on this scenario, we plot an azimuthally averaged, background-subtracted radial surface-density profile in the right panel of Figure 4. This consists of the stars shown as gray points in the CMD of Figure 2, binned in elliptical annuli with the measured ellipticity of Tri II. The overplotted red line is an exponential profile with $r_h = 2′.5$ as derived from our maximum likelihood analysis, with the cyan dashed curve representing the King model fit. Both model fits reproduce the density profile well to densities nearly two orders of magnitude below the background level. The lack of a "break" in the surface-density profile may be further evidence that Tri II has not recently suffered any tidal disruption.

4.2.1. Tri II's Orbit and its Dynamical Status

Its position and large radial velocity ($\langle v_{\mathrm{GSR}} \rangle = -264$ km s^{-1}; Kirby et al. 2017) imply that Tri II must be on a rather radial orbit, approaching its pericenter. The lack of obvious tidal debris is perhaps not surprising—the "break" radius in the stellar density profile of a disrupting satellite drifts monotonically to larger radii after its minimum immediately after pericenter (e.g., Łokas et al. 2013), such that any debris stripped on the previous pericentric passage have drifted far from the satellite by now. The narrow main sequence seen in Figure 2 suggests that the dwarf is also not extended along the
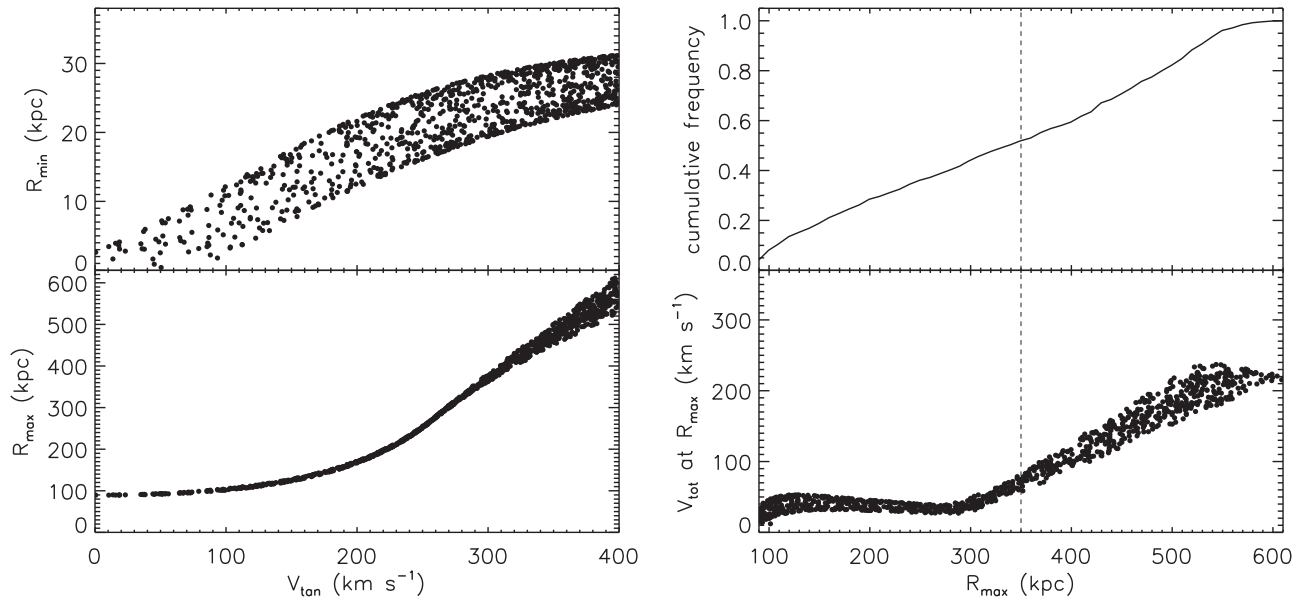
Figure 6. Results from 1000 orbit simulations for Tri II. Orbits were integrated for ± 2 Gyr, starting with the known v_{GSR}, position, and distance of Tri II, and random tangential velocities of $|V_{tan}| < 400$ km s^{-1}. Left panels: minimum Galactocentric distance (R_{min}; equivalent to the pericenter for a bound orbit) in the forward evolution of the orbit (upper panel), and maximum distance (R_{max}; i.e., apocenter for bound orbits; lower panel) in the previous 2 Gyr. Many of the bound orbits approach the innermost regions of the Galaxy, while the minimum apocenter distance is ~ 95 kpc. Right panels: cumulative distribution of the maximum distance reached in the simulated orbits, and the total Galactocentric velocity at each R_{max} (which should be small for bound orbits). The vertical line at $R = 350$ kpc represents the approximate virial radius of the Milky Way (note that the velocities in the lower panel begin to rise near $R_{max} \gtrsim 300$ kpc, suggesting that 350 kpc is a conservative estimate of the virial radius for our adopted potential). A total of 510 out of 1000 (or 51%) of the orbits have $R_{max} > 350$ kpc, meaning that more than half of the simulated Tri II orbits are unbound (assuming a MW virial radius of 350 kpc).

line of sight. To confirm this, we measured the standard deviation about the NGC 7078 ridgeline for main sequence stars within 3′ of Tri II, and between $21 < i_0 < 24$. The scatter is $\sigma_{i_0} = 0.06$ mag, equal to roughly ± 0.8 kpc width about the mean distance. However, this does not account for the contribution of unresolved binaries to the main sequence width, nor the ± 1.6 kpc uncertainty in the distance itself. We thus conclude that we have not detected any line of sight extension of Tri II.

We next consider what we can learn from the position and radial velocity of Tri II about its orbit. To do so, we generate 1000 random tangential velocity vectors that are perpendicular to the direction of the velocity vector implied by v_{GSR}, and have magnitude $|V_{tan}| < 400$ km s^{-1} ($V_{tan} = 400$ km s^{-1} would yield a total 3D Galactocentric velocity of 477 km s^{-1} for Tri II, which exceeds the predicted Milky Way escape velocity at the distance of Tri II; see, e.g., Figure 9 of Kafle et al. 2014). For each of the 1000 3D velocity vectors created by combining the radial velocity with V_{tan}, we integrate an orbit starting from the position of Tri II for ± 3 Gyr in the Galactic potential of Johnston (1998).[17] Figure 6 (left panels) shows the minimum Galactocentric distance reached in the forward orbit integration (i.e., the pericenter for a bound orbit), and the maximum distance (apocenter if the satellite is bound) in the previous 2.0 Gyr, as a function of the total tangential velocity. As expected, the orbits are rather radial, with eccentricities between $0.75 < e < 0.99$. A number of the orbits pass very

near the Galactic center. In the right panel of Figure 6 we show the cumulative distribution of the maximum distance, R_{max}. More than half (51%) of the orbits have $R_{max} > 350$ kpc (i.e., greater than the approximate MW virial radius), suggesting that Tri II could be on its first infall into the Milky Way's virial halo (though the good match of a King model to the surface-density profile may suggest that the Galactic potential has imposed a truncation to the radial extent of Tri II, which could argue against the first-infall scenario). We also note that $V_{tan} \gtrsim 300$ km s^{-1} leads to unbound orbits; thus, we expect that if Tri II is bound to the MW, it should have a total proper motion of $\mu_{total} < \frac{V_{tan}}{4.74 d}$, or $\mu_{total} < 2.23$ mas yr^{-1} (assuming a distance of 28.4 kpc). The RGB of Tri II may be within reach of *Gaia*, for which expected proper motion uncertainties are $\lesssim 0.3$ mas per star at $G = 20$ (Perryman et al. 2001),[18] while LSST will achieve $\lesssim 0.5$ mas per star accuracy at $r \sim 23$ (e.g., LSST Science Collaboration et al. 2009), well below the turnoff of Tri II.

With these simulated orbits in hand, we can assess the possible tidal interaction of Tri II within the Galactic potential. In Figure 7 we show the distribution of tidal radii of Tri II at pericenter for the 1000 simulated orbits. Tidal radii (for a logarithmic Galactic potential) are calculated using the formula of Oh et al. (1995):

$$r_{tidal} = a \left[\frac{M_{sat}}{M_{Gal}} \right]^{1/3}$$
$$\times \left\{ \frac{(1-e)^2}{[(1+e)^2/2e]\ln[(1+e)/(1-e)]+1} \right\}^{1/3}, \quad (1)$$

---

[17] The gravitational potential implemented by Johnston (1998) includes a Miyamoto-Nagai disk (Miyamoto & Nagai 1975), a Hernquist (1990) spheroid, and a logarithmic halo. Had we instead used the NFW halo potential of Bovy (2015) or McMillan (2017), our results would be qualitatively similar, given that the difference between accelerations in the NFW and logarithmic halos is small in the outer regions of the Milky Way. Our arbitrary choice of potential was meant only to guide our intuition, and not to definitively "fit" the orbital behavior of Tri II.

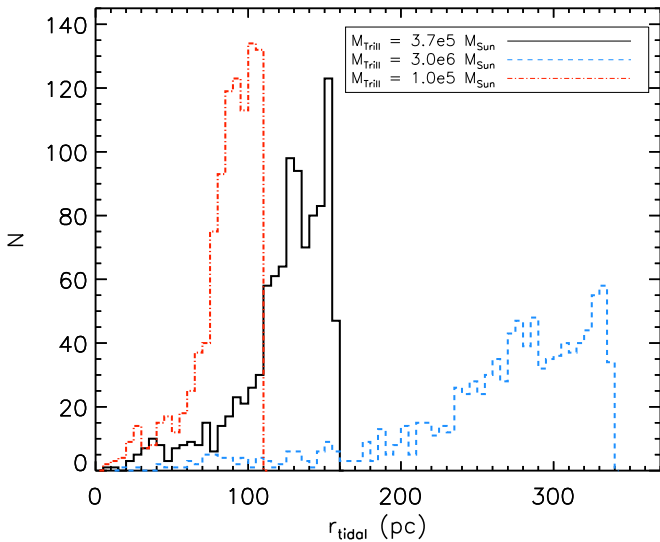[18] https://www.cosmos.esa.int/web/gaia/science-performance

Figure 7. Distribution of tidal radii at pericenter for the 1000 simulated orbits of Tri II, assuming three different masses for the dwarf. The tidal radius is smaller than the observed extent of Tri II (e.g., Figure 4) and our measured King tidal radius of $r_t = 97 \pm 27$ pc only for the lowest mass progenitor (and a small fraction of the intermediate mass simulated UFDs).

where a and e are the orbital semimajor axis and eccentricity, respectively, M_{sat} is the satellite's total mass, and M_{Gal} is the mass of the Milky Way within the semimajor axis. We calculate M_{Gal} using

$$M_{Gal}(r) \approx 1.1 \times 10^{10} \left(\frac{r}{1 \text{ kpc}} \right) M_\odot, \qquad (2)$$

from Burkert (1997), assuming $v_{circ,MW} = 220$ km s^{-1}. Because the mass of Tri II is uncertain, we choose three values:[19] (i) $M_{TriII} = 3.7 \times 10^5 M_\odot$ (black histogram), corresponding to the upper limit from Kirby et al. (2017); (ii) $M_{TriII} = 3.0 \times 10^6 M_\odot$ (Martin et al. 2016; blue dashed histogram[20]); and a low mass (iii) $M_{TriII} = 1.0 \times 10^5 M_\odot$ (red, dotted–dashed histogram). Recall that the stellar density in Figure 4 shows no break from an exponential profile out to ~90 pc, where it blends with the background density. Furthermore, our King model maximum likelihood fits to the stellar density profile yield a tidal radius of 97 ± 27 pc for Tri II. If the mass of Tri II is as low as $10^5 M_\odot$, Figure 7 suggests that its tidal radius would be less than 90 pc for nearly all simulated orbits, in which case we might expect to see tidal debris (assuming the surface brightness of the debris was within reach of our observations).[21] For the more massive simulated satellites, few of the tidal radii are smaller than 90 pc, suggesting that even if

---

[19] Note that these literature values, which are based on measured velocity dispersions using, e.g., the method of Wolf et al. (2010), correspond to the mass within the half-light radius. Thus the total mass of Tri II, if it has a significant DM halo, is likely much larger, which would make our estimates of the tidal radii lower limits.

[20] Even though this mass estimate has been superseded by that of Kirby et al. (2017), we have included it for completeness, as the true velocity dispersion of Tri II is still unknown.

[21] Note that assuming a V-band stellar mass-to-light ratio of 2 $M_\odot/L_{V,\odot}$, our measured luminosity of Tri II ($L_V \sim 260 L_\odot$) corresponds to a stellar mass of $M_{*,TriII} \sim 520 M_\odot$. A DM-free satellite with this stellar mass would have tidal radii 5.8 times smaller than those of the $1 \times 10^5 M_\odot$ satellite shown in Figure 7, and would thus be highly susceptible to tidal disruption.

Tri II is on a bound orbit, it is unlikely to suffer significant tidal disruption. Understanding the puzzling Tri II system thus depends critically on resolving its stellar velocity dispersion to accurately derive its mass.

5. H I Upper Limits

We searched for atomic gas reservoirs in Col I and Tri II in publicly available data from the southern hemisphere Galactic All Sky Survey (McClure-Griffiths et al. 2009) and northern hemisphere Effelsberg Bonn H I Survey (EBHIS; Winkel et al. 2016), respectively. We find no H I emission peaks that are statistically significant at the 5σ level along the line of sight to either dwarf when the data are smoothed to a spectral resolution of 15 km s^{-1}. Adopting the distances to Col I and Tri II determined in Section 3, the corresponding 5σ, single-channel upper limits on the H I mass $M_{H I}$ and on the relative gas content $M_{H I}/L_V$ are given in Table 1.

We note that we find an unresolved emission peak at lower statistical significance (3.5σ) along the line of sight to Tri II at $V_{helio} \sim -395$ km s^{-1} in the smoothed EBHIS data. This velocity differs by only ~15 km s^{-1} from the systemic velocity of the dwarf measured from stellar kinematics (Kirby et al. 2017). Given the presence of similar peaks across the 20 deg^2 EBHIS datacube containing the Tri II line of sight as well as the detection of high-velocity Galactic H I features and gas associated with M31 at similar velocities in this region (Wakker & van Woerden 1997; Kerp et al. 2016), we conclude that this peak is unlikely to stem from a gas reservoir in Tri II.

While these H I upper limits do not place constraints on the neutral gas content that are as strong as those derived by Spekkens et al. (2014) for other MW dwarfs, they are consistent with the overall lack of H I in *all* dwarf spheroidals observed within the MW virial radius (see Figure 2 of Spekkens et al. 2014). Given the lack of obvious young stellar populations in either Col I or Tri II, it is likely that the two systems do not contain significant reservoirs of gas.

6. Discussion and Conclusions

We present deep Subaru/HSC imaging of Milky Way companions Col I and Tri II, from which we derive the structural parameters (summarized in Table 1) and map the stellar density fields around these two satellites (Figure 3). Our deep photometry reaching beyond the MSTO of Col I, at a distance of $d_{Col I} = 183 \pm 10$ kpc, shows this satellite to have properties consistent with most Galactic UFDs. It is apparently made up of an old, metal-poor stellar population, including a prominent BHB (see Figure 1), which we use to estimate the distance to Col I. We find $M_V = -4.2 \pm 0.2$ for Col I, and a half-light radius of $r_h = 117 \pm 17$ pc, placing it directly on the observed size–luminosity relation for Local Group dwarfs (Figure 5). The stellar density map of Col I shows no evidence of obvious distortions or tidal disruption. We also search archival data for evidence of neutral hydrogen in Col I, and derive an upper limit of $M_{H I} < 1.2 \times 10^4 M_\odot$, and $M_{H I}/L_V < 3.1 M_\odot/L_\odot$. Overall, Col I appears to be typical of old, metal-poor, gas-free UFDs in the Milky Way, but currently resides at a large distance from the Galaxy.

We derive a distance to Tri II of $d_{Tri II} = 28.4 \pm 1.6$ kpc via least-squares fitting of >3 mag of the resolved main sequence. Tri II's stellar population is well-matched by the empirical ridgeline of old, metal-poor GC NGC 7078 (from Bernard

et al. 2014), as expected from its measured spectroscopic metallicity of $\langle[\mathrm{Fe/H}]\rangle = -2.24$ (Kirby et al. 2017). Tri II is extremely faint, with $M_V = -1.2 \pm 0.4$ (or $L_V \sim 260\,L_\odot$), and compact ($r_h = 21 \pm 4$ pc). The stellar density map of Tri II is of particular interest, because one possible solution to its higher metallicity relative to the Local Group relation at its measured M_V (e.g., Kirby et al. 2017) is that Tri II may have been more massive/luminous in the past, but suffered tidal mass loss. We see no evidence of tidal debris in either the stellar density map (Figure 3) or radial stellar density profile (Figure 4). We search archival H I observations near Tri II, and find upper limits of $M_{\mathrm{H\,I}} < 3.1 \times 10^2\,M_\odot$ and $M_{\mathrm{H\,I}}/L_V < 1.2\,M_\odot/L_\odot$. Both this and the Col I upper limit are consistent with the lack of observed H I in all dSphs within the MW virial radius (Spekkens et al. 2014), though not particularly stringent limits on their neutral gas content.

We further explore the dynamical state of Tri II via a suite of orbital simulations based on its position and radial velocity, for 1000 different values of its tangential velocity. We find that more than half of the simulated orbits place Tri II on its first infall into the MW potential. If so, the atypical properties of Tri II relative to other UFDs may be due to different environmental effects. The surface-density profile of Tri II is well matched by an exponential profile, with no evidence for tidal debris in the form of a break in the profile at large radii. We show that the predicted tidal radii from our simulated orbits are larger than the observed extent of Tri II for all but the lowest mass satellites. We additionally find that Tri II has a present-day stellar MF similar to those of other UFDs, in contrast to the flatter MFs typical of GCs (which arise due to dynamical evolution, and, in some cases, preferential loss of low-mass stars to tidal stripping). Taken together, the evidence we have presented in this work suggests that Tri II is a dwarf galaxy with no evidence of being affected by tides.

In this contribution, we have presented deep Subaru/HSC observations of Milky Way satellites Columba I and Triangulum II. Col I has properties typical of MW ultra-faint dwarfs, and Tri II has properties more like a dwarf galaxy than a GC. Our work highlights the precision that can be attained in measurements of UFD structural parameters with high-quality, deep photometry reaching $\gtrsim 2$ mag deeper than previous data sets. In addition, with the large field of view covered by our HSC imaging, we find no evidence for the presence of significant tidal debris within several tidal radii of each of these dwarfs (within our surface-brightness limits).

ORCID iDs

Jeffrey L. Carlin ⓘ https://orcid.org/0000-0002-3936-9628
David J. Sand ⓘ https://orcid.org/0000-0003-4102-380X
Kristine Spekkens ⓘ https://orcid.org/0000-0002-0956-7949
Beth Willman ⓘ https://orcid.org/0000-0003-2892-9906
Denija Crnojević ⓘ https://orcid.org/0000-0002-1763-4128
Evan Kirby ⓘ https://orcid.org/0000-0001-6196-5162
Annika H. G. Peter ⓘ https://orcid.org/0000-0002-8040-6785
Aaron J. Romanowsky ⓘ https://orcid.org/0000-0003-2473-0369
Jay Strader ⓘ https://orcid.org/0000-0002-1468-9668

References

Abazajian, K. N., Adelman-McCarthy, J. K., Agüeros, M. A., et al. 2009, ApJS, 182, 543
Aihara, H., Armstrong, R., Bickerton, S., et al. 2017, arXiv:1702.08449
Alam, S., Albareti, F. D., Allende Prieto, C., et al. 2015, ApJS, 219, 12
Albert, A., Anderson, B., Bechtol, K., et al. 2017, ApJ, 834, 110
Amorisco, N. C. 2017, ApJ, 844, 64
Aparicio, A., & Gallart, C. 2004, AJ, 128, 1465
Astropy Collaboration, Robitaille, T. P., Tollerud, E. J., et al. 2013, A&A, 558, A33
Beasley, M. A., Romanowsky, A. J., Pota, V., et al. 2016, ApJL, 819, L20
Bechtol, K., Drlica-Wagner, A., Balbinot, E., et al. 2015, ApJ, 807, 50

Belokurov, V., Zucker, D. B., Evans, N. W., et al. 2006, ApJL, 647, L111
Belokurov, V., Zucker, D. B., Evans, N. W., et al. 2007, ApJ, 654, 897
Bernard, E. J., Ferguson, A. M. N., Schlafly, E. F., et al. 2014, MNRAS, 442, 2999
Bosch, J., Armstrong, R., Bickerton, S., et al. 2017, arXiv:1705.06766
Bovy, J. 2015, ApJS, 216, 29
Brandt, T. D. 2016, ApJL, 824, L31
Brown, T. M., Tumlinson, J., Geha, M., et al. 2012, ApJL, 753, L21
Burkert, A. 1997, ApJL, 474, L99
Carlin, J. L., Sand, D. J., Price, P., et al. 2016, ApJL, 828, L5
Carretta, E., Bragaglia, A., Gratton, R. G., et al. 2009, A&A, 505, 117
Chambers, K. C., Magnier, E. A., Metcalfe, N., et al. 2016, arXiv:1612.05560
Contenta, F., Balbinot, E., Petts, J. A., et al. 2017a, arXiv:1705.01820
Contenta, F., Gieles, M., Balbinot, E., & Collins, M. L. M. 2017b, MNRAS, 466, 1741
Crnojević, D., Sand, D. J., Zaritsky, D., et al. 2016, ApJL, 824, L14
Dark Energy Survey Collaboration 2005, arXiv:astro-ph/0510346
Dark Energy Survey Collaboration, Abbott, T., Abdalla, F. B., et al. 2016, MNRAS, 460, 1270
Dotter, A., Chaboyer, B., Jevremović, D., et al. 2008, ApJS, 178, 89
Drlica-Wagner, A., Bechtol, K., Allam, S., et al. 2016, ApJL, 833, L5
Drlica-Wagner, A., Bechtol, K., Rykoff, E. S., et al. 2015, ApJ, 813, 109
Drlica-Wagner, A. & MagLiteS Team 2017, in APS April Meeting Abstracts, #J5.001
Flewelling, H. A., Magnier, E. A., Chambers, K. C., et al. 2016, arXiv:1612.05243
Forbes, D. A., & Kroupa, P. 2011, PASA, 28, 77
Geha, M., Brown, T. M., Tumlinson, J., et al. 2013, ApJ, 771, 29
Hernquist, L. 1990, ApJ, 356, 359
Huang, S., Leauthaud, A., Murata, R., et al. 2017, arXiv:1705.01599
Hunter, J. D. 2007, CSE, 9, 90
Ivezic, Z., Tyson, J. A., Abel, B., et al. 2008, arXiv:0805.2366
Johnston, K. V. 1998, ApJ, 495, 297
Jurić, M., Kantor, J., Lim, K., et al. 2015, arXiv:1512.07914
Kafle, P. R., Sharma, S., Lewis, G. F., & Bland-Hawthorn, J. 2014, ApJ, 794, 59
Kerp, J., Kalberla, P. M. W., Ben Bekhti, N., et al. 2016, A&A, 589, A120
Kim, D., & Jerjen, H. 2015, ApJL, 808, L39
Kim, D., Jerjen, H., Mackey, D., Da Costa, G. S., & Milone, A. P. 2015, ApJL, 804, L44
King, I. 1962, AJ, 67, 471
Kirby, E. N., Cohen, J. G., Guhathakurta, P., et al. 2013, ApJ, 779, 102
Kirby, E. N., Cohen, J. G., Simon, J. D., et al. 2017, ApJ, 838, 83
Kirby, E. N., Cohen, J. G., Simon, J. D., & Guhathakurta, P. 2015, ApJL, 814, L7
Koda, J., Yagi, M., Yamanoi, H., & Komiyama, Y. 2015, ApJL, 807, L2
Koposov, S. E., Belokurov, V., Torrealba, G., & Evans, N. W. 2015, ApJ, 805, 130
Laevens, B. P. M., Martin, N. F., Bernard, E. J., et al. 2015a, ApJ, 813, 44
Laevens, B. P. M., Martin, N. F., Ibata, R. A., et al. 2015b, ApJL, 802, L18
Landsman, W. B. 1993, in ASP Conf. Ser. 52, Astronomical Data Analysis Software and Systems II, ed. R. J. Hanisch, R. J. V. Brissenden, & J. Barnes (San Francisco, CA: ASP), 246

Łokas, E. L., Gajda, G., & Kazantzidis, S. 2013, MNRAS, 433, 878
LSST Science Collaboration, Abell, P. A., Allison, J., et al. 2009, arXiv:0912.0201
Magnier, E. A., Schlafly, E. F., Finkbeiner, D. P., et al. 2016, arXiv:1612.05242
Martin, N. F., de Jong, J. T. A., & Rix, H.-W. 2008, ApJ, 684, 1075
Martin, N. F., Ibata, R. A., Collins, M. L. M., et al. 2016, ApJ, 818, 40
Martin, N. F., Nidever, D. L., Besla, G., et al. 2015, ApJL, 804, L5
McClure-Griffiths, N. M., Pisano, D. J., Calabretta, M. R., et al. 2009, ApJS, 181, 398
McConnachie, A. W. 2012, AJ, 144, 4
McMillan, P. J. 2017, MNRAS, 465, 76
Miyamoto, M., & Nagai, R. 1975, PASJ, 27, 533
Miyazaki, S., Komiyama, Y., Nakaya, H., et al. 2012, Proc. SPIE, 8446, 84460Z
Muñoz, R. R., Carlin, J. L., Frinchaboy, P. M., et al. 2006, ApJL, 650, L51
Muñoz, R. R., Geha, M., & Willman, B. 2010, AJ, 140, 138
Muñoz, R. R., Padmanabhan, N., & Geha, M. 2012, ApJ, 745, 127
Nidever, D. L., Olsen, K., Walker, A. R., et al. 2017, AJ, 154, 199
Oh, K. S., Lin, D. N. C., & Aarseth, S. J. 1995, ApJ, 442, 142
Peñarrubia, J., Navarro, J. F., & McConnachie, A. W. 2008, ApJ, 673, 226
Perez, F., & Granger, B. E. 2007, CSE, 9, 21
Perryman, M. A. C., de Boer, K. S., Gilmore, G., et al. 2001, A&A, 369, 339
Rockosi, C. M., Odenkirchen, M., Grebel, E. K., et al. 2002, AJ, 124, 349
Sand, D. J., Olszewski, E. W., Willman, B., et al. 2009, ApJ, 704, 898
Sand, D. J., Strader, J., Willman, B., et al. 2012, ApJ, 756, 79
Schlafly, E. F., & Finkbeiner, D. P. 2011, ApJ, 737, 103
Schlegel, D. J., Finkbeiner, D. P., & Davis, M. 1998, ApJ, 500, 525
Shanks, T., Metcalfe, N., Chehade, B., et al. 2015, MNRAS, 451, 4238
Simon, J. D., & Geha, M. 2007, ApJ, 670, 313
Spekkens, K., Urbancic, N., Mason, B. S., Willman, B., & Aguirre, J. E. 2014, ApJL, 795, L5
Taylor, M. B. 2005, in ASP Conf. Ser. 347, Astronomical Data Analysis Software and Systems XIV, ed. P. Shopbell, M. Britton, & R. Ebert (San Francisco, CA: ASP), 29
Torrealba, G., Koposov, S. E., Belokurov, V., & Irwin, M. 2016, MNRAS, 459, 2370
van der Walt, S., Colbert, S. C., & Varoquaux, G. 2011, CSE, 13, 22
van Dokkum, P., Abraham, R., Brodie, J., et al. 2016, ApJL, 828, L6
Venn, K. A., Starkenburg, E., Malo, L., Martin, N., & Laevens, B. P. M. 2017, MNRAS, 466, 3741
Wakker, B. P., & van Woerden, H. 1997, ARA&A, 35, 217
Walsh, S. M., Jerjen, H., & Willman, B. 2007, ApJL, 662, L83
Willman, B., Dalcanton, J. J., Martinez-Delgado, D., et al. 2005, ApJL, 626, L85
Willman, B., & Strader, J. 2012, AJ, 144, 76
Winkel, B., Kerp, J., Flöer, L., et al. 2016, A&A, 585, A41
Wolf, J., Martinez, G. D., Bullock, J. S., et al. 2010, MNRAS, 406, 1220
York, D. G., Adelman, J., Anderson, J. E., Jr., et al. 2000, AJ, 120, 1579
Zaritsky, D. 2017, MNRAS, 464, L110
Zucker, D. B., Belokurov, V., Evans, N. W., et al. 2006a, ApJL, 650, L41
Zucker, D. B., Belokurov, V., Evans, N. W., et al. 2006b, ApJL, 643, L103